Photocatalytic degradation of aqueous rhodamine B by TiO$_2$/ZnO/rGO nanocomposite: photocatalytic activity and catalytic mechanism

Lu Peng[a], Peng Nian[a], Jingwei Feng[a,b],*, Xiangxiang Han[a], Binhua Cui[a], Songsheng Lu[c], Jie Zhang[c], Chenming Li[c], Aiyong Zhang[a]

[a]*Department of Municipal Engineering, School of Civil and Hydraulic Engineering, Hefei University of Technology, Hefei 230009, China, Tel. +86-551-62904144; Fax: +86-551-62904144; email: jingweifeng@hfut.edu.cn (J.W. Feng)*
[b]*Nanjing University & Yancheng Academy of Environmental Protection Technology and Engineering, Yancheng 224001, China*
[c]*PLA Army Academy of Artillery and Air Defense, Hefei 230031, China*

ABSTRACT

A novel nanocatalyst, TiO$_2$/ZnO/rGO, was successfully synthesized by hydrothermal method and characterized with X-ray diffractometer, Brunauer–Emmett–Teller, scanning electron microscopy, transmission electron microscopy, Fourier transform infrared, X-ray photoelectron spectroscopy and Raman spectra. The photocatalytic activities of the as-obtained nanocatalyst were investigated based on the degradation of rhodamine B (RhB) under UV irradiation. The results showed that the TiO$_2$/ZnO/rGO nanocatalyst could significantly improve the degradation efficiency of RhB when the mass ratio of TiO$_2$ to ZnO was 5:1 and the GO content was 5%. An approximately 100% of photocatalytic degradation of RhB in 90 min was achieved at 5 mg L^{-1} of initial RhB concentration, 150 mg L^{-1} of TiO$_2$/ZnO/rGO dosage and 8.5 of pH under UV light irradiation. The photocatalytic degradation of RhB was well fitted to the pseudo-first-order kinetic equation. Photocatalytic degradation of RhB by TiO$_2$/ZnO/rGO nanocatalyst mainly attributed to the reactive species of O$_2^{\bullet-}$, $^\bullet$OH and HO$_2^\bullet$. Moreover, the degradation intermediates of RhB were detected by GC-MS and the photocatalytic degradation mechanism for RhB was proposed. N-deethylation, conjugate structure destruction, ring opening and hydroxylation were involved in the photocatalytic degradation process of RhB.

Keywords: Photocatalysis; TiO$_2$/ZnO/rGO nanocatalyst; Hydrothermal method; Photocatalytic activity; Catalytic mechanism

1. Introduction

Nowadays, the control and treatment of water pollution have been a common concern in the world. Over the past decades, large quantities of dyes, especially from textile, printing and paper industries, were discharged into the environment, which has become one of the important sources of water pollution. In addition, synthetic dyes were widely used in food, pharmaceutical and cosmetic industries [1]. With the widespread use of various synthetic dyes, their harmfulness has gradually been recognized. In order to meet the needs of consumers, these dye products were developing in the direction of anti-photolysis and anti-oxidation, making it difficult to be degraded in the natural environment, affecting the normal life activities of aquatic animals and plants, and destroying the ecological balance of aquatic environment. And the synthetic dyes were mostly toxic substances, and had carcinogenicity and teratogenicity [2]. In addition, various contaminants such as toxic organic compounds and heavy metals further exacerbated this problem, and removal of these contaminants from water systems was a priority to ensure a safe and clean environment [3]. In order to effectively control and treat water pollution, diverse methods and materials for environmental remediation were developed [4–6].

Rhodamine B (RhB), one of the most commonly used synthetic dyes, also known as rose bengal B, or alkaline rose

* Corresponding author.

essence, was a synthetic dye with fresh pink color [7]. It was mainly used in the paper industry for dyeing wax paper, typed paper, glossy paper, also in laboratories, cosmetics and other industries. It was once used as food additive, however, now it was not allowed to be used for food dyeing because of the carcinogenic function [8].

At present, various techniques have been used to treat dye-containing water such as physical adsorption, ozone oxidation, high voltage discharge plasma, photocatalysis and biological decomposition [9–11]. In recent years, photocatalytic technology has attracted widespread attention in the removal of organic matter from wastewater [12]. Sharma et al. [13] studied the photoremediation of malachite green by multifunctional nanocomposite pectin thorium (IV) tungstomolybdate. Photoremediation of toxic dye from aqueous environment using monometallic and bimetallic quantum dots based nanocomposites was also reported [14]. Among various semiconductor photocatalysts, TiO_2 has become the focus of scholars' research owing to its physicochemical properties, non-toxicity, low cost, excellent optical and electrical properties [15]. However, since the forbidden band width of TiO_2 was about 3.2 eV, the utilization rate of solar energy was low, and the photogenerated electron–hole pair recombination rate was high, resulting in the reduction of the catalytic activity [16]. Compared with TiO_2, ZnO was also an excellent n-type semiconductor and had good photoelectric properties [17]. In addition, the conduction band and valence band of ZnO were more negative than TiO_2. Many studies have shown that the heterojunction between TiO_2 and ZnO caused the electrons on the conduction band of ZnO transfer to the conduction band of TiO_2, thereby reducing the recombination rate of electron–hole pairs and improving the photocatalytic efficiency [18].

Graphene (GO) was a new type of lamellar material composed of two-dimensional honeycomb lattice closely packed. It had excellent electrical and mechanical properties and could be used as an excellent electron transport material in photocatalytic process, which was used widely to improve the photocatalytic performance of the catalyst [19]. Xu et al. studied the photocatalytic properties and mechanism of ZnO/GO composites, the results showed that the ZnO/GO photocatalysts exhibited enhanced photocatalytic activity for the degradation of organic dyes. In addition, the excellent photocatalytic activity was attributed to the high migration efficiency of photoinduced electrons and the suppression of charge carrier recombination, owing to the electronic interaction between ZnO and GO [20].

Presently, there were many researches on ZnO/GO, ZnO/TiO_2, TiO_2/GO composites [18,19,21]; however, studies on nanocatalyst prepared by combining TiO_2, ZnO and GO were rarely reported before. In this paper, the TiO_2/ZnO/rGO nanocatalyst was prepared by hydrothermal method, and the GO was converted to reduced graphene (rGO) during the materials preparation process. The synthesized TiO_2/ZnO/rGO nanocatalyst was characterized by X-ray diffractometer (XRD), scanning electron microscopy (SEM), transmission electron microscopy (TEM), Fourier transform infrared (FT-IR), X-ray photoelectron spectroscopy (XPS) and Raman spectra. The photocatalytic degradation performance of RhB by TiO_2/ZnO/rGO nanocatalyst under UV light was studied. The effect of various factors and the content of GO in

the composite materials was also discussed. In addition, the changes of pH and conductivity in the degradation process were evaluated. Furthermore, the photocatalytic degradation intermediates of RhB were determined by gas chromatography-mass spectrometry (GC-MS), the degradation pathways and degradation mechanism were speculated.

2. Materials and methods

2.1. Materials

RhB (purity ≥ 95.0%) was purchased from Aladdin Industrial Corporation, China. And the structural formula of RhB is shown in Fig. S1. Titanium dioxide, zinc acetate, graphite powder, concentrated sulfuric acid, sodium nitrate, hydrochloric acid, potassium permanganate, hydrogen peroxide and ammonia were all purchased from Sinopharm Chemical Reagent Co., Ltd., China. Deionized water was used in the present work. All chemicals were used as received without further purification.

2.2. Preparation of GO

The modified Hummers' method was used to prepare GO [22–25]. 120 mL of concentrated H_2SO_4 was added into the round bottom flask, and it was cooled to 0°C–5°C in an ice bath. 5 g of graphite powder and 2.5 g of $NaNO_3$ were mixed and then added to the round bottom flask, keeping stirring vigorously to dissolve completely. Then 15 g $KMnO_4$ was added slowly into the mixture solution and kept stirring for 2.5 h with temperature 10°C–15°C. The round bottom flask was then placed in a 35°C-water bath for 30 min. After the reaction was completed, an appropriate amount of deionized water was added while stirring, and the temperature was controlled between 80°C and 100°C, reacting for 30 min. The solution was diluted with warm deionized water and a small amount of H_2O_2 was added. The obtained suspension was thoroughly washed, first with 5% HCl solution and then with deionized water, until the supernatant pH reached 7. The washed solution was lyophilized in a freeze dryer to obtain GO.

2.3. Preparation of TiO_2/ZnO nanocomposites

0.5 g of TiO_2 powder was dispersed in 20 mL of absolute ethanol, which was dispersed by ultrasound for 30 min, solution A was obtained. 0.271 g of $Zn(CH_3COO)_2$ was dissolved in 10 mL of water to obtain solution B (mass ratio of TiO_2 to ZnO was 5:1). Solution B was added into solution A and then the suspension was stirred for 1 h. Then appropriate amount of $NH_3 \cdot H_2O$ was added into the mixture solution to adjust the pH = 9. Sequentially, the mixture solution was transformed into a 100 mL polytetrafluoroethylene reactor, keeping for 10 h at 200°C. And the obtained solid was thoroughly washed with deionized water and then dried to get TiO_2/ZnO nanocomposites.

2.4. Preparation of TiO_2/ZnO/rGO nanocatalyst

Different amount of GO was dispersed in 50 mL deionized water by ultrasound for 1 h, solution A was obtained, the content of GO in the composite material was controlled

to 5%, 10% and 20%, respectively. 0.5 g of TiO_2 powder was dispersed in 20 mL of absolute ethanol, which was dispersed by ultrasound for 30 min, solution B was obtained. Solution B was added into solution A with stirring for 1 h to obtain solution C. Then, 0.271 g of $Zn(CH_3COO)_2$ was dissolved in 10 mL of water to obtain solution D. Solution D was added into liquid C, stirring for 1 h. Then appropriate amount of $NH_3 \cdot H_2O$ was added into the mixture solution to adjust the pH to 9. Sequentially, the mixture solution was transformed into a 100 mL polytetrafluoroethylene reactor, keeping for 10 h at 200°C. And the obtained solid was thoroughly washed with deionized water and then dried to obtain TiO_2/ZnO/rGO nanocatalyst (the content of GO in the composite material was 5%, 10% and 20%, respectively).

2.5. Experimental instruments and methods

The photocatalytic reaction apparatus used in this study is shown in Fig. S2. The UV lamp used in the experimental setup was a mercury lamp (14 W). RhB stock solution (100 mg L^{-1}) was prepared, and a certain amount of stock solution was diluted to obtain RhB work solution. The catalyst was added into the solution with stirring. Prior to the photocatalytic reaction, the suspension was placed under dark conditions and magnetically stirred for 30 min to achieve the adsorption–desorption equilibrium. The suspension was then exposed to UV light, keeping stirring to provide uniform contact of the catalyst and RhB.

2.6. Characterization method

The crystal structure of the prepared TiO_2/ZnO/rGO nanocatalyst was characterized by an XRD (X'Pert PRO MPD, PANalytical B.V., Netherlands) with scanning angle range of 3°–90° and scanning speed of 6°min^{-1}. The Brunauer–Emmett–Teller (BET) surface areas were obtained at –196°C using a specific surface area and porosity analyzer (ASAP2460, Micromeritics, USA). The morphology and structural characteristics of the composites were examined by field emission SEM (SU8020, Hitachi, Japan) and TEM (JEM 1200EX, JEOL, Japan). FT-IR spectra were obtained as KBr pellets using an FT-IR spectrometer (Nicolet 6700, Thermo Nicolet, USA). The microstructure of the composite was investigated using a microscopic confocal laser Raman spectrometer (HR Evolution, HORIBA Jobin Yvon, France). XPS (ESCALAB250Xi, Thermo, USA) was used to analyze the elemental species, chemical valence and relative content of the composite surface.

2.7. Analysis methods

The concentration of RhB was measured by a spectrophotometer (UV2600, UNICO, China) with a detection wavelength of 552 nm [26]. The degradation efficiency of RhB was calculated by Eq. (1).

$$R(\%) = \frac{C_0 - C}{C_0} \times 100\% \tag{1}$$

where R was the degradation efficiency of RhB (%), C was the residual concentration of RhB after treatment (mg L^{-1}) and C_0 was the initial concentration of RhB (mg L^{-1}).

The pH of the solution was determined with a pH meter (PHS-3C, Shanghai INESA Scientific Instrument Co., Ltd., China). The conductivity of the solution was measured by a conductivity meter (DDB-303A, Shanghai INESA Scientific Instrument Co., Ltd., China).

The degradation intermediates of RhB was detected by GC-MS. First, the sample (10 mL) was dried in a freeze dryer for 48 h, then dissolved in 5 mL of DMF and filtered through a 0.22 μm cellulose ester membrane. 100 μL of BSTFA was added to the filtrate, which was sealed and derivatized in an oven at 70°C for 1 h, and then the treated samples were determined by GC-MS. The column used in the GC-MS system was a HP-5 capillary column (30.0 m × 320 μm × 0.25 μm, Agilent, USA). The carrier gas was high-purity helium (99.999%) at flow rate of 1 mL min^{-1}. The injection was splitless and the injection volume was 1 μL. The inlet temperature, source temperature and the transmission line temperature were set at 250°C, 250°C and 280°C, respectively. The column temperature ramp-up procedure was as follows: 60°C for 3 min, 8°C min^{-1} to 300°C, holding for 5 min at 300°C. Mass spectrometry was performed using a full-range ion scan mode (m/z 35–500). The ionization source was an ion source and the electron energy was 70 eV.

3. Results and discussion

3.1. Characterization

3.1.1. XRD

The crystallographic structure of the prepared TiO_2/ZnO/rGO nanocatalyst was analyzed by XRD, and the results are shown in Fig. 1. It can be seen from Fig. 1 that the diffraction peaks were sharp, indicating that the composite material had good crystallinity. And by comparing with the XRD standard map of anatase type TiO_2 (JCPDS No. 21-1272), it was found that the matching degree was very high. The diffraction peaks of the prepared TiO_2/ZnO/rGO nanocatalyst at 2θ values of 25.3°, 37.8°, 48.0°, 53.9°, 55.1° and 62.7° could be indexed as the (101), (004), (200), (105), (211) and (204)
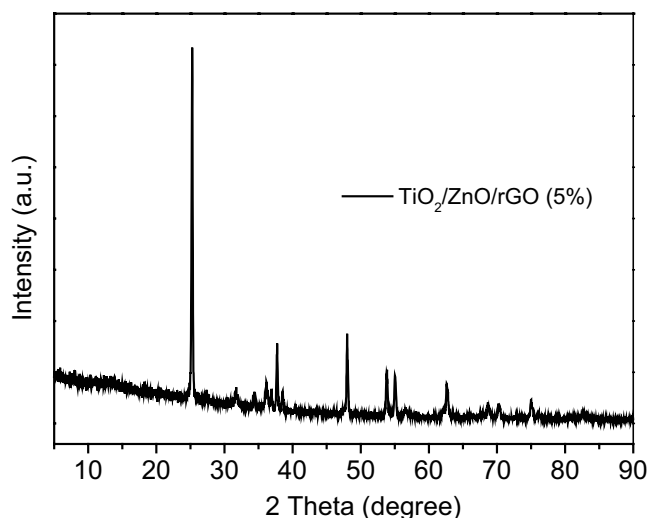

Fig. 1. XRD patterns of TiO_2/ZnO/rGO nanocatalyst.

structure planes of the anatase TiO$_2$ (JCPDS No. 21-1272), respectively. The (101) crystal plane with the highest peak intensity was the main crystal plane structure of anatase TiO$_2$, indicating that TiO$_2$ in the prepared TiO$_2$/ZnO/rGO nanocatalyst mainly existed in the anatase crystal form. In addition, the peaks at 2θ values of 31.8°, 34.3°, 36.3° and 56.6° corresponded to the (100), (002), (101) and (110) structure planes of the red zinc ore crystal ZnO (JCPDS No. 36-1451), respectively. It was indicated that ZnO in the prepared TiO$_2$/ZnO/rGO nanocatalyst mainly existed wurtzite structure. The peak at 2θ value of 26° corresponded to the graphite (002) surface diffraction peak, but the spectra of the material had a very weak peak only at 2θ value of 23°, indicating that most of the GO was converted to rGO during the preparation of the nanocatalyst [27].

The crystallite dimension of TiO$_2$ and ZnO in the TiO$_2$/ZnO/rGO nanocatalyst was calculated by the Scherrer formula Eq. (2); the calculation results are shown in Table S1.

$$D = \frac{K\gamma}{B\cos\theta} \qquad (2)$$

where K was the Scherrer constant ($K = 0.89$), D was the average thickness of the crystal grains perpendicular to the crystal plane direction, B was the half-height width of the diffraction peak of the measured sample, θ was the diffraction angle, and γ was the X-ray wavelength (γ = 0.15418 nm).

As shown in Table S1, crystallite dimension of TiO$_2$ and ZnO in the TiO$_2$/ZnO/rGO nanocatalyst was 38 and 31 nm, respectively.

3.1.2. BET

N$_2$ adsorption–desorption measurements were conducted to examine specific surface area and porous structure of the TiO$_2$/ZnO/rGO nanocatalyst. As shown in Fig. S3, the curve exhibited the prominent characteristic of type-IV isotherms with a H$_3$ hysteresis loop, indicating the existence of mesopores (2–50 nm) [16]. And the isotherms showed higher adsorptions at the high relative pressure range of 0.8–1.0, demonstrating the large volumes of mesopores and macropores [28]. The BET surface area, pore volume and pore size of the TiO$_2$/ZnO/rGO nanocatalyst were presented in Table S2. As displayed in Table S2, the TiO$_2$/ZnO/rGO nanocatalyst showed a small BET surface area of 5.72 m^2 g^{-1} and an average pore size of 29.78 nm, which was consistent with the calculation results of Scherrer formula Eq. (2).

3.1.3. SEM and TEM

The SEM and TEM images of the prepared TiO$_2$/ZnO/rGO nanocatalyst are shown in Figs. 2 and 3. As presented in Fig. 2, the rGO surface was cross-linked and exhibited a sheet-like structure, and agglomerates (TiO$_2$ and ZnO particles) were observed adhering to the rGO surface. The sheet-like pleat structure of rGO and the solid spherical particles (TiO$_2$ and ZnO) attached can be clearer observed from Fig. 3.

3.1.4. Raman spectra and FT-IR spectra

Raman spectra of different materials are shown in Fig. 4. Anatase phase TiO$_2$ exhibit tetragonal crystal structure and
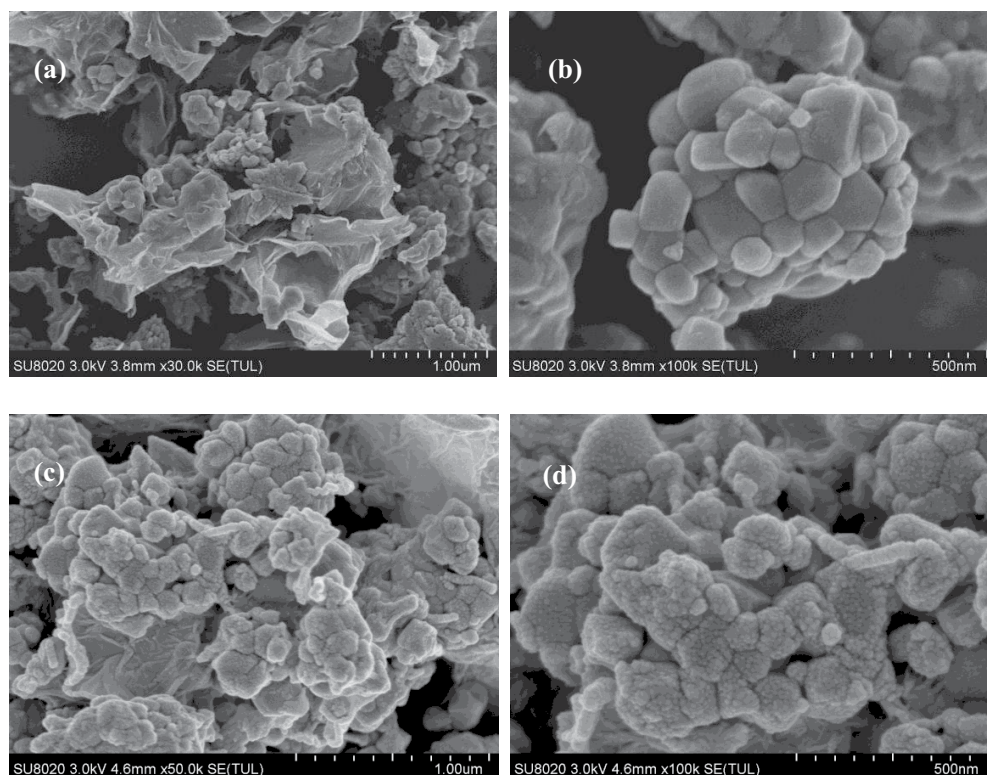

Fig. 2. SEM images of TiO$_2$/ZnO/rGO nanocatalyst before ((a) and (b)) and after photodegradation ((c) and (d)).
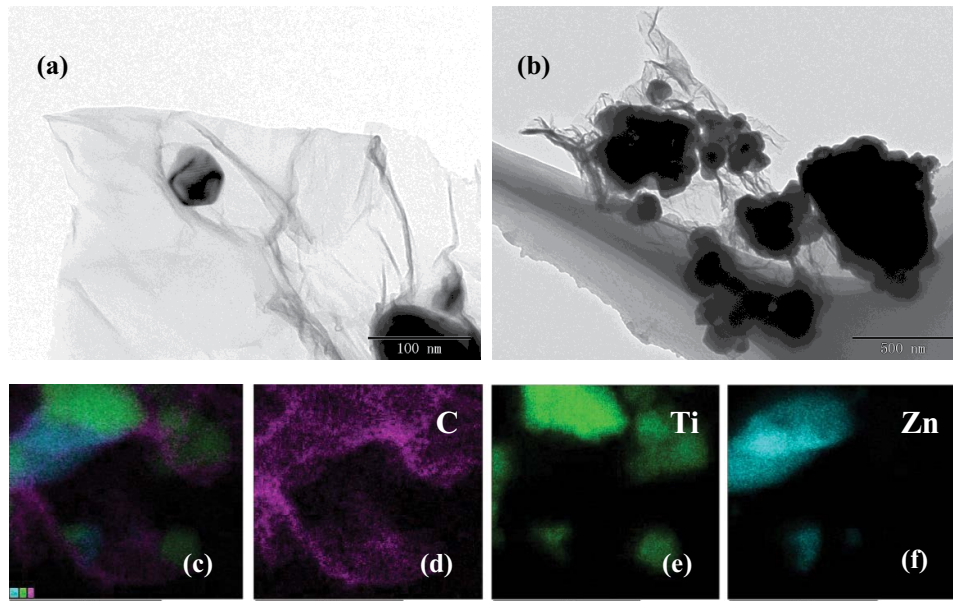
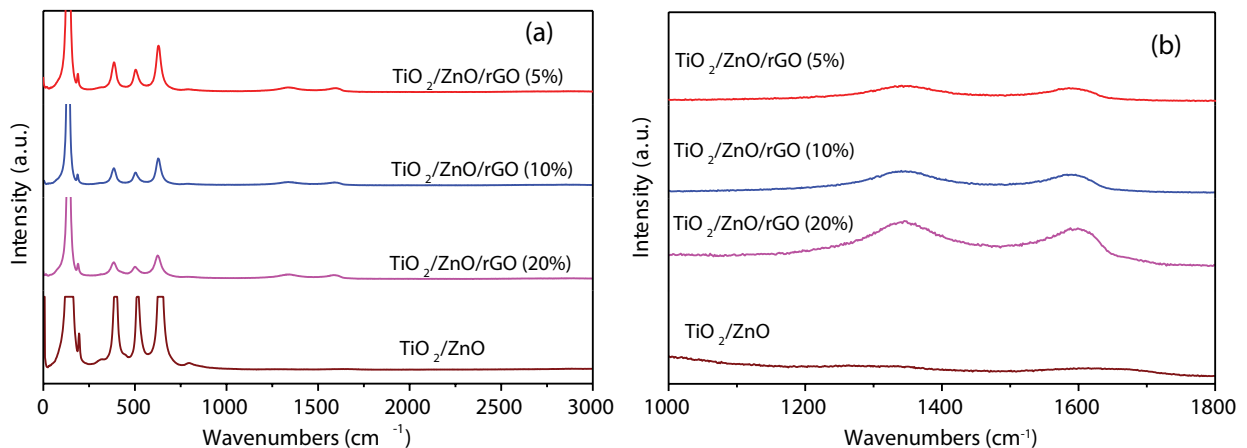Fig. 3. TEM ((a) and (b)) and TEM–EDS ((c)–(f)) images of TiO_2/ZnO/rGO nanocatalyst.

Fig. 4. Raman spectra of different materials.

belong to the space group D_{4h} (I41 amd⁻¹). And each unit cell contained two TiO_2 unites with six Raman active modes $A_{1g} + 2B_{1g} + 3E_g$, which was confirmed in the first-order Raman spectrum of single crystal TiO_2 [29]. The Raman spectra of all samples exhibited peaks centered at 144, 197, 399, 516 and 639 cm⁻¹ assigned all to TiO_2 anatase phase. The peak with the highest intensity at 143 cm⁻¹ could be attributed to the symmetric type variable angular vibration of O–Ti–O. The Raman peaks at 197 and 640 cm⁻¹ corresponded to the $E_{g(2)}$ and $E_{g(3)}$ modes, respectively [30]. The peak of 516 cm⁻¹ could be assigned to the A_{1g} mode. The Raman peak at 399 cm⁻¹ was attributed to the $B_{1g(1)}$ mode [30,31]. As shown in Fig. 4b, the bands appeared at about 1,350 and 1,600 cm⁻¹ could be assigned to the well documented bands of disordered amorphous carbon (D band) and ordered sp²-bonded carbon atoms (G band), respectively. In addition, Fig. 4b showed that as the GO content in the material increased,

the peak corresponding to the anatase phase TiO_2 gradually weakened, but the peak corresponding to GO gradually increased. The above analysis indicated that TiO_2 was present in the composite material in the anatase form, and the GO existed in the reduced state.

FT-IR spectra of the TiO_2/ZnO/rGO nanocatalyst are shown in Fig. 5. As shown in the figure, the peak intensity increased gradually with the increase of GO contents. The peaks at 550 and 700 cm⁻¹ were observed and they were almost at the same intensity, which could be assigned to symmetric stretching vibration of the Ti–O–Ti bond and O–Ti–O flexion vibration, respectively [32]. A broad peak was detected at around 3,250 cm⁻¹, which was corresponded to the absorption peak of the –OH stretching vibration on the surface of the material [32]. For the FT-IR spectra of all the composites, the band at 1,575 cm⁻¹ was observed, which was the C–C skeletal vibration of the rGO layers [21].

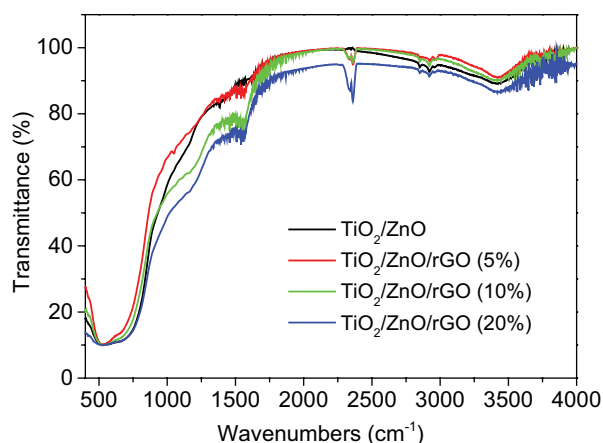Fig. 5. FT-IR spectra of different materials.

3.1.5. XPS

In order to further investigate the composition of the prepared $TiO_2/ZnO/rGO$ nanocatalyst, XPS analysis was carried out. Fig. 6 shows the XPS spectra of the $TiO_2/ZnO/rGO$ nanocatalyst. The XPS survey spectra showed that the peaks appearing at 284.88, 459.35, 530.76 and 1,022.53 eV corresponded to C1s, Ti2p, O1s and Zn2p, respectively. The XPS spectra of C1s are displayed in Fig. 6b, the peaks at about 284.6, 285.7 and 288.6 eV corresponded to C–C, C–OH and C=O, respectively. The peak ascribed to C–C was more intense than that of C=O, indicating the reduction of GO in the preparation process of the materials [33]. Fig. 6c showed the high-resolution XPS spectrum of O1s, which involved two characteristic peaks attributing to the lattice oxygen of TiO_2 surface (530.6 eV) and the hydroxyl group (532.2 eV), respectively [34]. As shown in Fig. 6d, two peaks were observed at 459.3 and 464.9 eV, corresponding to the $Ti2p_{3/2}$ and $Ti2p_{1/2}$, respectively [21]. The band

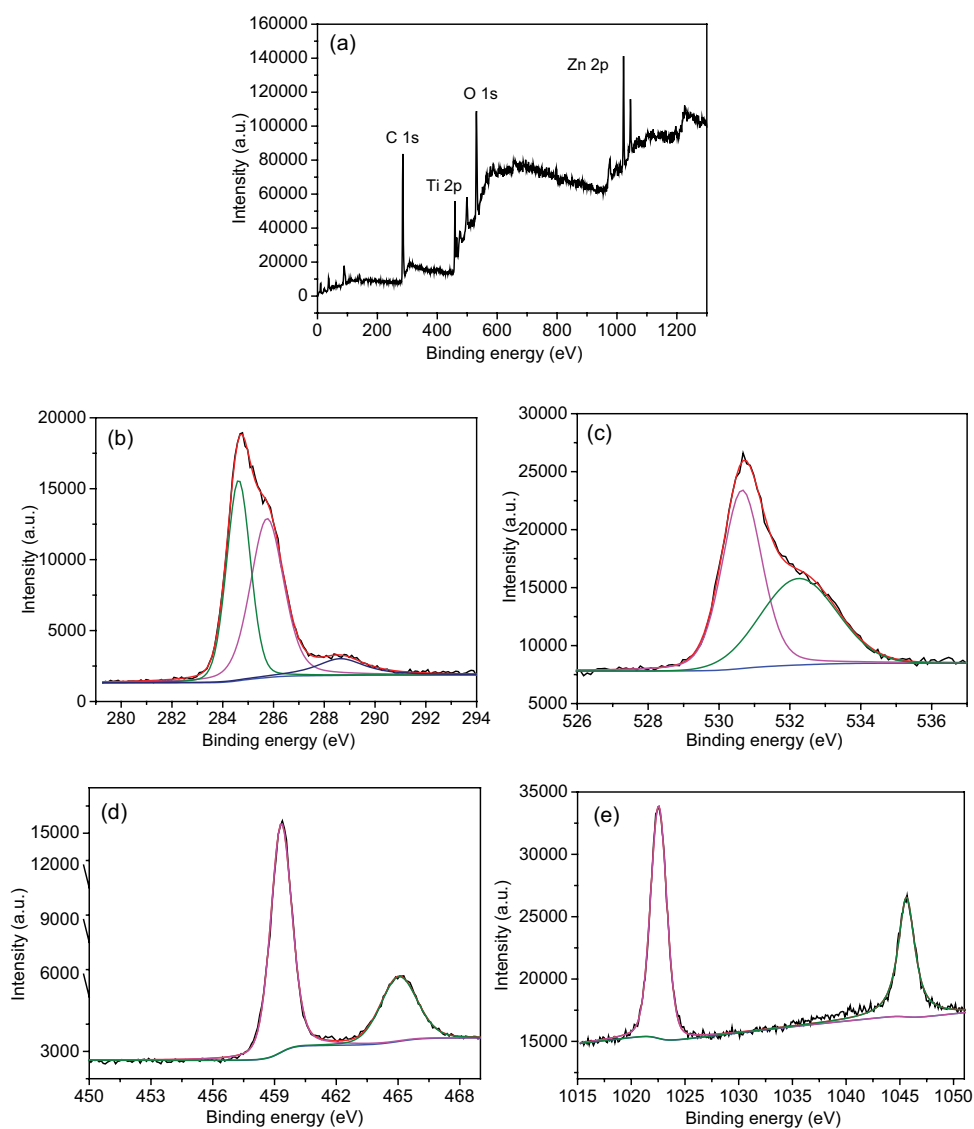Fig. 6. (a) XPS survey spectra of $TiO_2/ZnO/rGO$ nanocatalyst, (b) the C1s XPS spectra of $TiO_2/ZnO/rGO$ nanocatalyst, (c) the O1s XPS spectra of $TiO_2/ZnO/rGO$ nanocatalyst, (d) the Ti2p XPS spectra of $TiO_2/ZnO/rGO$ nanocatalyst, (e) the Zn2p XPS spectra of $TiO_2/ZnO/rGO$ nanocatalyst.

gap difference between the two peaks was calculated to be 5.6 eV, which indicated the presence of Ti^{4+} in the TiO_2/ZnO/rGO nanocatalyst [35]. The XPS spectra of Zn2p are displayed in Fig. 6e, the peaks at 1,022.5 and 1,045.6 eV corresponded to $Zn2p_{3/2}$ and $Zn2p_{1/2}$, respectively.

3.2. Catalytic mechanism

Fig. 7 displays the catalytic degradation mechanism of RhB by TiO_2/ZnO/rGO nanocatalyst under UV irradiation. As shown in Fig. 7, a large amount of photogenerated electrons and holes were produced when the TiO_2/ZnO/rGO nanocatalyst were irradiated by UV light. And the heterojunction between TiO_2 and ZnO caused the electrons to transfer from conduction band of ZnO to that of TiO_2. Such an efficient charge separation reduced the recombination of the hole–electron pairs and increased the lifetime of the charge carriers, thus increasing the quantum efficiency [34]. In addition, rGO could serve as an electron acceptor and transporter for photocatalytic processes with excellent electron conduction properties [36]. A portion of the photogenerated electrons were transferred to the surface of the rGO, further promoting efficient separation of electrons and holes [37]. Photogenerated electrons generated by UV excitation could react with O_2 to produce $O_2^{\bullet-}$, and holes could react with H_2O to form $^\bullet OH$. Besides, some $O_2^{\bullet-}$ reacted with H^+ to form $HO_2^\bullet$. $O_2^{\bullet-}$, $^\bullet OH$ and $HO_2^\bullet$ with high oxidability could decompose RhB into small molecules (Eqs. (3)–(7)) [38].

$$TiO_2 + hv \rightarrow TiO_2\left(e^-\right) + TiO_2\left(h^+\right) \tag{3}$$

$$ZnO + hv \rightarrow ZnO\left(e^-\right) + ZnO\left(h^+\right) \tag{4}$$

$$H_2O + h^+ \rightarrow H^+ + {}^\bullet OH \tag{5}$$

$$O_2 + e^- \rightarrow O_2^{\bullet-} \tag{6}$$

$$O_2^{\bullet-} + H^+ \rightarrow HO_2^\bullet \tag{7}$$

3.3. Photocatalytic activity and factors affecting photocatalytic degradation process

Moradi et al. [32] studied the photocatalytic activity of TiO_2/ZnO nanocatalyst prepared with different molar ratios, the results revealed that the photocatalytic activity of TiO_2/ZnO nanocatalyst with ratio of 5:1 was the best. Therefore, the ratio of TiO_2 to ZnO was 5:1 in the present work, and the effect of GO content on the photocatalytic activity of TiO_2/ZnO/rGO nanocatalyst was investigated. As shown in Fig. 8a, the degradation efficiencies of RhB by TiO_2 and TiO_2/ZnO at 90 min were 60% and 80%, respectively, suggesting that the incorporation of ZnO greatly improved the photocatalytic activity of TiO_2. And with the addition of GO, the photocatalytic degradation efficiency of RhB for the TiO_2/ZnO/rGO nanocatalyst was further improved and reached almost 100% at 90 min. In addition, with the increasing of the GO content from 5% to 20%, the photocatalytic activity of the TiO_2/ZnO/rGO nanocatalyst displayed little difference. In the first half hour, the degradation efficiency of RhB increased slightly with the increase of GO content, and then the degradation efficiency of RhB was basically the same.

As shown in Fig. 8a, without the UV irradiation, the concentration of RhB decreased slowly with increasing reaction time. And the adsorption of RhB was enhanced slightly with the increasing content of rGO (from 5% to 20%) in the catalyst. In addition, the concentration of RhB only decreased by 7% within 90 min, demonstrating that the catalyst had little adsorption capacity and photocatalytic degradation was the main removal mechanism of RhB. In case of synergistic process, the adsorption of RhB onto the photocatalyst surface and generation of electron–hole pairs were occurred, the adsorption of RhB onto photocatalyst facilitated the photodegradation process and increased the degradation rate of RhB [39].

The effect of catalyst dosage on the degradation of RhB is shown in Fig. 8b. It can be seen from Fig. 8b that the degradation efficiency of RhB increased gradually with the increasing TiO_2/ZnO/rGO dosage. As the TiO_2/ZnO/rGO dosage increased, the dispersed catalyst particles in the solution
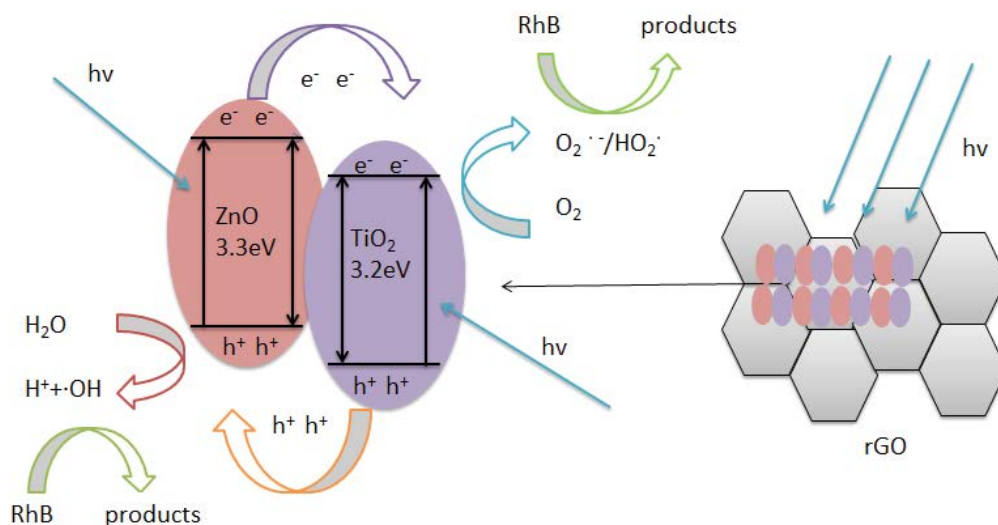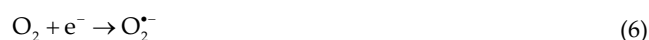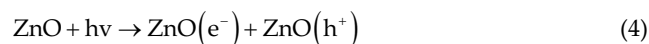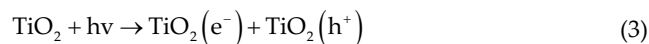

Fig. 7. Catalytic degradation mechanism of RhB in aqueous solution by TiO_2/ZnO/rGO nanocatalyst under UV irradiation.
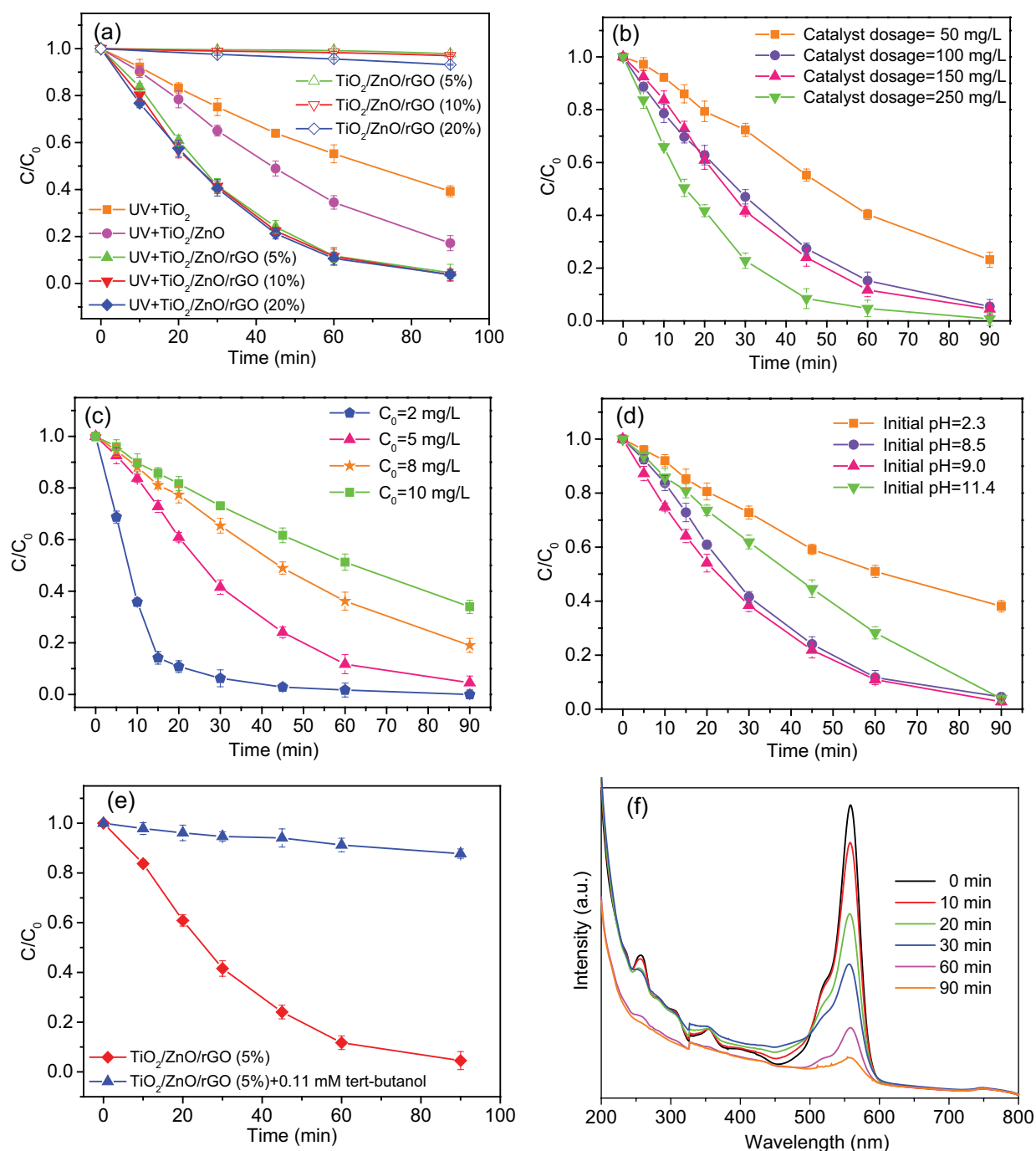
Fig. 8. Effect of catalyst composition (a), catalyst dosage (b), initial concentration of RhB (c), initial pH (d) and tert-butanol (e) on the degradation of RhB; UV visible spectra variations during the degradation of RhB (f) (Experimental conditions: (a) 298 K, C_0 = 5 mg L^{-1}, TiO$_2$/ZnO = 5:1, pH = 8.5, TiO$_2$/ZnO/rGO = 150 mg L^{-1}; (b) 298 K, C_0 = 5 mg L^{-1}, TiO$_2$/ZnO = 5:1, wt.%(rGO) = 5%, pH = 8.5; (c) 298 K, TiO$_2$/ZnO/rGO = 150 mg L^{-1}, TiO$_2$/ZnO = 5:1, wt.% (rGO) = 5%, pH = 8.5; (d) 298 K, C_0 = 5 mg L^{-1}, TiO$_2$/ZnO/rGO = 150 mg L^{-1}, TiO$_2$/ZnO = 5:1, wt.% (rGO) = 5%; (e) 298 K, C_0 = 5 mg L^{-1}, TiO$_2$/ZnO = 5:1, wt.% (rGO) = 5%, pH = 8.5, TiO$_2$/ZnO/rGO = 150 mg L^{-1}; (f) 298 K, C_0 = 5 mg L^{-1}, TiO$_2$/ZnO = 5:1, wt.% (rGO) = 5%, pH = 8.5, TiO$_2$/ZnO/rGO = 150 mg L^{-1}).

also increased, leading to the improvement in the contact probability of catalyst with RhB and the increase of the reactive species generated by UV photocatalysis. Thus, the degradation efficiency of RhB was promoted. When the dosage of the catalyst increased from 50 to 100 mg L^{-1}, the degradation efficiency of RhB was remarkably improved (increased by

17% at 90 min). However, with the catalyst dosage increasing continuously, the degradation efficiency of RhB was only slightly increased, indicating that the catalyst dosage was basically saturated. In addition, the increase of the catalyst dispersed in the solution might cause poor light permeability affecting the degradation of RhB.

Fig. 8c presents the effect of initial concentration of RhB on the degradation of RhB. As shown in Fig. 8c, when the initial concentrations of RhB were 2, 5, 8 and 10 mg L⁻¹, the corresponding degradation efficiencies of RhB were 100%, 95%, 81% and 66% at 90 min, respectively. The degradation efficiency of RhB increased from 66% to 100% with the initial concentration of RhB reduced from 10 to 2 mg L⁻¹. And the degradation efficiency of RhB increased significantly with decreasing initial concentration of RhB. The amount of catalyst and reactive species generated in the photocatalysis system was almost constant under the same experimental conditions. The RhB molecules at lower initial concentration could sufficiently contact with the catalyst. While with the increase of the initial concentration of RhB, the RhB molecules were denser in the solution, and the competition for the active sites and the reactive species was also intensified. In addition, the photodegradation intermediates of RhB were also involved in the competition. Therefore, the degradation efficiency of RhB decreased with the increasing initial concentration of RhB.

The pH generally had a remarkable impact on the degradation of organic contaminants by changing the environment of the photocatalytic reaction system. The effect of pH on the photodegradation of pollutants was generally associated with the surface ionization state, valence and conduction bands, agglomeration ability of the photocatalyst and the radical formation [40]. As presented in Fig. 8d, the degradation efficiency of RhB only reached 60% at pH = 2.3 in 90 min, and the degradation efficiency of RhB was suppressed in acid conditions. However, the degradation efficiency of RhB increased under neutral and alkaline conditions, and almost reached 100% at 90 min. In addition, as the alkalinity of the system was further enhanced (pH = 11.4), the photocatalytic degradation efficiency of RhB reduced. Therefore, the neutral and slightly alkaline environment was more suitable for the photocatalytic degradation of RhB by TiO₂/ZnO/rGO nanocatalyst.

Tert-butanol was added to the reaction system to investigate the role of $^\bullet$OH in the degradation of RhB by TiO₂/ZnO/rGO nanocomposite. As shown in Fig. 8e, the degradation of RhB was obviously inhibited with the addition of tert-butanol, manifesting the important role of $^\bullet$OH in the degradation of RhB. The UV–Visible spectra of photocatalytic degradation of RhB are shown in Fig. 8f. It can be seen from Fig. 8f that the absorption intensity decreased gradually with the increasing reaction time at about 552 nm. And degradation of RhB reached 100% within 90 min, indicating that the TiO₂/ZnO/rGO catalyst could degrade RhB effectively under UV conditions.

Table 1 exhibited the comparisons of the performance for the photocatalytic degradation of RhB in this work and previous studies. As illustrated in Table 1, better performance for the degradation of RhB by using the TiO₂/ZnO/rGO was observed.

3.4. Degradation kinetics analysis

The experimental data were fitted using the pseudo-first-order kinetic model Eq. (8) [49,50].

$$\ln\frac{C_0}{C} = kt \tag{8}$$

Table 1
Comparisons of the performance and rate constant k for the photocatalytic degradation of RhB

Catalyst	Catalyst dosage (mg L⁻¹)	C_0 (mg L⁻¹)	Initial pH	Irradiation source	T	k (min⁻¹)	Performance		Reference
							t (min)	R (%)	
TiO₂/ZnO/rGO (5%)	250	5	8.5	14 W UVA lamp	298 K	0.054	60	95	This study
TiO₂/ZnO/rGO (5%)	150	5	8.5	14 W UVA lamp	298 K	0.036	90	100	This study
ZnO nanoparticles	480	5	–	15 W Hg-lamp	–	0.006	300	62	[41]
Bi₂WO₆	500	10	–	300 W xenon lamp	–	0.081	35	98	[42]
PW₁₁O₃₉Fe(III)(H₂O)⁴⁻	68	4.79	7.0	200 W metal halide lamp	–	0.062	80	100	[43]
N-doped titanate nanotubes	1,000	5	7.0	100 W Hg lamp	–	0.024	120	100	[44]
N4%–ZnO	1,000	4.79	7.0	1000 W xenon lamp	–	0.028	150	98	[45]
SnO₂ quasi-nanospheres	200	10	–	500 W xenon lamp	–	0.032	60	82	[46]
120°C-Bi₂WO₆	1,000	5	–	500 W xenon lamp	–	0.053	60	100	[47]
Ag/TiO₂	2,000	10	–	500 W mercury lamp	288 K	0.023	180	98	[48]

Note: C_0 was the initial concentration of RhB (mg L⁻¹); R was the degradation efficiency of RhB (%); k was the rate constant (min⁻¹); t was the irradiation time (min); T was the temperature of the solution (K).

where C_0 was the initial concentration of RhB (mg L^{-1}), C was the concentration of RhB after treated (mg L^{-1}), k was the apparent rate constant (min^{-1}). The apparent rate constant k was chosen as the basic kinetic parameter for comparison of the photocatalytic activities. As shown in Table 2, the data were well fitted to the pseudo-first-order kinetic equation, indicating that the photocatalytic degradation of RhB by TiO$_2$/ZnO/rGO nanocatalyst under UV irradiation belonged to the pseudo-first-order reaction kinetics. According to the pseudo-first-order kinetic theory, the rate constant k was independent of the initial concentration of RhB [51]. However, the data in Table 2 show that the rate constant k decreased with increasing initial concentration of RhB. In the reaction system of photocatalytic degradation of RhB by TiO$_2$/ZnO/rGO nanocatalyst, the degradation of RhB mainly depended on the reactive species (O$_2^{\bullet-}$, $^{\bullet}$OH and HO$_2^{\bullet}$). And more the reactive species (O$_2^{\bullet-}$, $^{\bullet}$OH and HO$_2^{\bullet}$) were produced with the increase of the TiO$_2$/ZnO/rGO nanocatalyst. In consequence, the rate constant k gradually increased with the increasing catalyst dosage [49,52–54]. In addition, the amount of

O$_2^{\bullet-}$, $^{\bullet}$OH and HO$_2^{\bullet}$ produced in the system remained basically constant with the experimental conditions unchanged. However, the amount of O$_2^{\bullet-}$, $^{\bullet}$OH and HO$_2^{\bullet}$ was relatively reduced with the increase of the initial concentration of RhB. Furthermore, the degradation intermediates of RhB also participated in the reaction, competing for the reactive species. Therefore, the rate constant k gradually decreased with the increasing initial concentration of RhB. In addition, the data in Table 2 display that the maximum and the minimum rate constants were 0.110 and 0.011 min^{-1}, respectively. The maximum rate constant was 10 times of the minimum rate constant. Comparisons of the rate constant k for the photocatalytic degradation of RhB are shown in Table 1; and higher rate constant k for the degradation of RhB by using the TiO$_2$/ZnO/rGO nanocatalyst was observed.

3.5. Changes in pH and conductivity during RhB degradation

Fig. 9 shows the changes of pH and conductivity during photocatalytic degradation of RhB. The pH values showed a

Table 2
Kinetic parameters of pseudo-first-order degradation kinetics under different factors

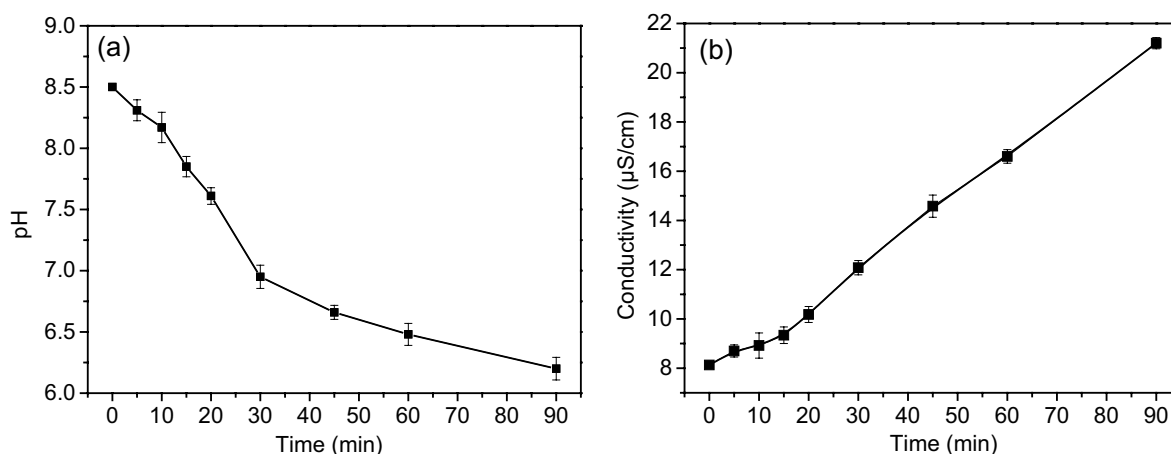| Factors	Catalyst dosage (mg L^{-1})	Initial concentration of RhB (mg L^{-1})	Initial pH	Rate constant k (min^{-1})	Half-life time $t_{1/2}$ (min)	R^2
Catalyst dosage	50	5	8.5	0.016	43.31	0.98
	100	5	8.5	0.033	21.00	0.99
	150	5	8.5	0.036	19.25	0.99
	250	5	8.5	0.054	12.83	0.99
Initial concentration of RhB	150	2	8.5	0.110	6.30	0.87
	150	5	8.5	0.036	19.25	0.99
	150	8	8.5	0.018	3.75	0.99
	150	10	8.5	0.012	57.75	0.99
Initial pH	150	5	2.3	0.011	63.00	0.99
	150	5	8.5	0.036	19.25	0.99
	150	5	9.0	0.040	17.33	0.99
	150	5	11.4	0.033	21.00	0.89

Fig. 9. Changes of solution pH (a) and conductivity (b) in the process of RhB degradation (298 K, C_0 = 5 mg L^{-1}, TiO$_2$/ZnO/rGO = 150 mg L^{-1}, TiO$_2$/ZnO = 5:1, wt.%(rGO) = 5%, pH = 8.5).

downward trend, and the conductivity showed an upward trend with the increasing reaction time. And the pH value of the system decreased rapidly in the first 30 min, and the decreasing trend got slower later, which was consistent with the variation of the degradation efficiency of RhB. The system environment gradually transformed to acidic conditions and the conductivity continued to increase with the increasing reaction time, indicating that RhB was decomposed into small molecular weight organic acid, which increased the conductivity of the system. It is shown in Fig. 9b that the conductivity of the system increased slowly in the first 30 min and increased rapidly in the last 60 min, suggesting that the degradation intermediates with poor conductivity were gradually converted into small molecular products with good conductivity [55].

3.6. Reuse of the TiO₂/ZnO/rGO nanocatalyst

The photocatalytic activity of the TiO_2/ZnO/rGO nanocatalyst was evaluated by the cyclic degradation of RhB dye under UV irradiation (Fig. 10). After each reaction run, the TiO_2/ZnO/rGO nanocatalyst was separated from the reaction system and reused again. As displayed in Fig. 10, after four cycles, the degradation efficiency of RhB was about 88% at 90 min, indicating that the synthesized TiO_2/ZnO/rGO nanocatalyst was promising in wastewater treatment for the excellent stability.

3.7. Degradation intermediates and degradation pathways of RhB

In order to clarify the degradation pathways of RhB by the TiO₂/ZnO/rGO-UV system, the degradation intermediates of RhB during the reaction were detected by GC-MS. The structures, retention times and spectrum ions of the degradation intermediates identified by GC-MS are presented in Table 3. According to the detection results, the degradation pathways of RhB were proposed. As shown in Fig. 11, N-deethylation process mainly happened in the early stage of RhB degradation. When all the ethyl groups of RhB gradually were removed, the •OH produced in the system attacked
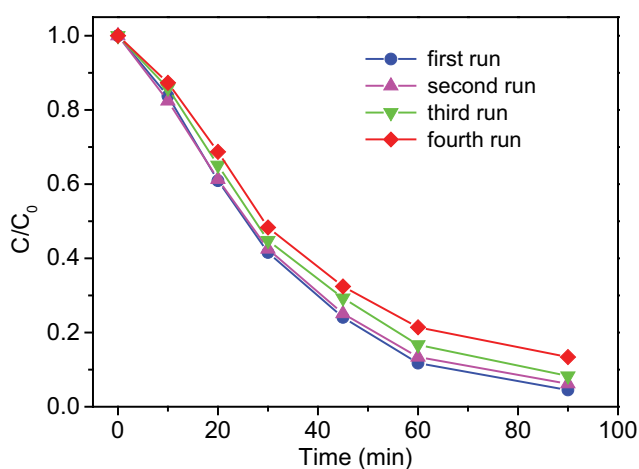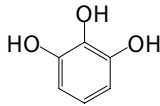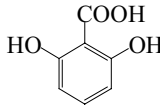
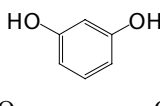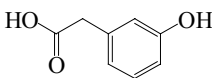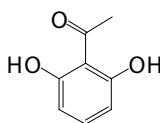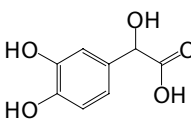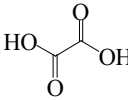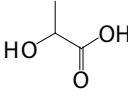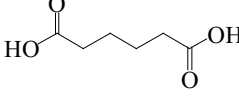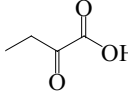Fig. 10. Reusing properties of the TiO₂/ZnO/rGO nanocatalyst (298 K, C_0 = 5 mg L⁻¹, TiO₂/ZnO/rGO = 150 mg L⁻¹, TiO₂/ZnO = 5:1, wt.%(rGO) = 5%, pH = 8.5).

Table 3
Structures, retention times and spectrum ions of the RhB degradation intermediates identified by GC-MS

No.	Proposed intermediates	Retention time (min)	Spectrum ions (m/z)
A		10.27	73
B		10.18	73, 355
C		10.54	73, 207
D		10.64	73, 115
E		10.66	73
F		12.91	281
G		10.23	73, 355
H		3.10	73, 147
I		8.57	73, 117, 147
J		21.23	44, 55, 100
K		9.93	57, 73

the RhB molecules, conjugate structure destruction, hydroxylation and ring opening reactions occurred, resulting in the generation of low molecular weight organic acid and alcohols. Subsequently, these degradation intermediates could be further oxidized and decomposed into CO_2 and H_2O. However, in the present work, the N-deethylated intermediates were not detected probably because of the chromatographic column used in the GC-MS detection process or the concentrations of the generated N-deethylated intermediates were lower than the detection limit of the method. Tao et al. [8] studied the
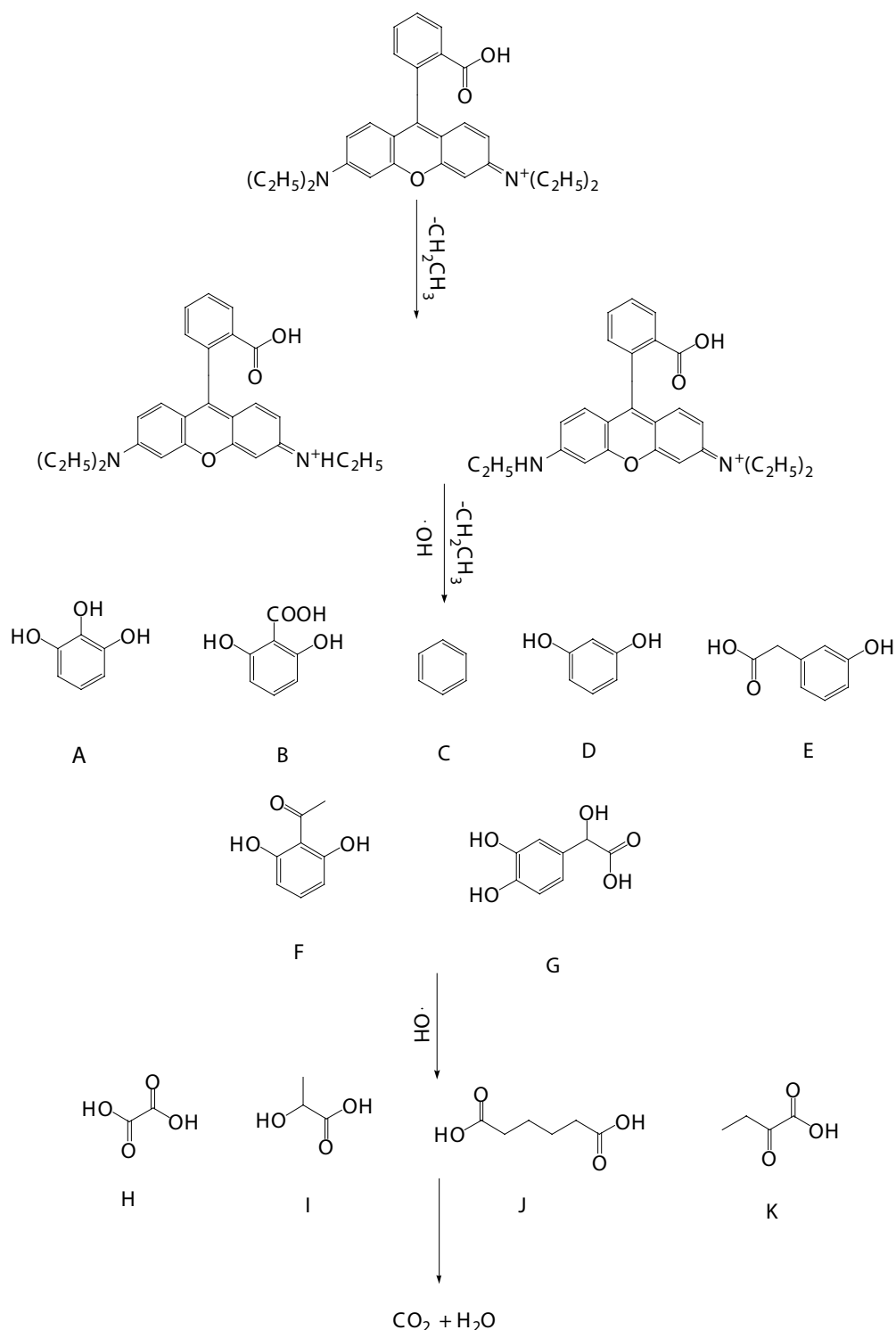
Fig. 11. Proposed degradation pathway of RhB.

removal performance of RhB in wastewater by coal-based carbon film combined with electric field and speculated the possible degradation pathway of RhB, the results indicated that RhB produced different N-deethylated intermediates, and these N-deethylated intermediates were further degraded into small molecular products by the cleavage of the conjugated structure, which finally were oxidized into CO_2 and H_2O. Hu et al. [56] studied the photocatalytic degradation of RhB by CdS/MIL-53(Fe) under visible light conditions, the predicted degradation pathway was basically consistent with that of Tao et al. [8]. Diao et al. [57] studied the degradation of RhB in pyrite/H_2O_2 and pyrite/persulfate (PS) Fenton

systems, the results demonstrated that the degradation of RhB was initiated by N-deethylation, chromophore cleavage and ring opening in both systems.

4. Conclusion

The $TiO_2/ZnO/rGO$ nanocatalyst synthesized by hydrothermal method had good photocatalytic properties. When the mass ratio of TiO_2 to ZnO was 5:1 and the GO content was 5%, the $TiO_2/ZnO/rGO$ nanocatalyst significantly improved the degradation efficiency of RhB. When the initial concentration of RhB was 5 mg L^{-1}, the dosage of the nanocatalyst was 150 mg L^{-1}, and the solution pH was 8.5, RhB was completely degraded under UV light in 90 min. The lower initial concentration of RhB, the alkaline system environment and the larger catalyst dosage were all favorable for the photocatalytic degradation of RhB. During the photocatalytic degradation of RhB by $TiO_2/ZnO/rGO$ nanocatalyst, the pH of the system gradually decreased and the conductivity gradually increased. Photocatalytic degradation of RhB by $TiO_2/ZnO/rGO$ nanocatalyst mainly attributes to the reactive species of $O_2^{\bullet-}$, $^{\bullet}OH$ and $HO_2^{\bullet}$. The degradation pathways for RhB included N-deethylation, conjugate structure destruction, ring opening and hydroxylation.

Acknowledgments

References

[1] J.S. Zhong, Q.Y. Wang, J. Zhou, D.Q. Chen, Z.G. Ji, Highly efficient photoelectrocatalytic removal of RhB and Cr(VI) by Cu nanoparticles sensitized TiO_2 nanotube arrays, Appl. Surf. Sci., 367 (2016) 342–346.

[2] K. He, G. Chen, G. Zeng, A. Chen, Z. Huang, J. Shi, T. Huang, M. Peng, L. Hu, Three-dimensional graphene supported catalysts for organic dyes degradation, Appl. Catal., B, 228 (2018) 19–28.

[3] G. Sharma, B. Thakur, Mu. Naushad, A. Kumar, F.J. Stadler, S.M. Alfadul, G.T. Mola, Applications of nanocomposite hydrogels for biomedical engineering and environmental protection, Environ. Chem. Lett., 16 (2018) 113–146.

[4] D. Pathania, G. Sharma, Mu. Naushad, V. Priya, A biopolymer-based hybrid cation exchanger pectin cerium(IV) iodate: synthesis, characterization, and analytical applications, Desal. Wat. Treat., 57 (2016) 468–475.

[5] M. Naushad, G. Sharma, A. Kumar, S. Sharma, A.A. Ghfar, A. Bhatnagar, F.J. Stadler, M.R. Khan, Efficient removal of toxic phosphate anions from aqueous environment using pectin based quaternary amino anion exchanger, Int. J. Biol. Macromol., 106 (2018) 1–10.

[6] A. Kumar, A. Kumar, G. Sharma, M. Naushad, F.J. Stadler, A.A. Ghfar, P. Dhiman, R.V. Saini, Sustainable nano-hybrids of magnetic biochar supported g-C_3N_4/FeVO$_4$ for solar powered degradation of noxious pollutants- synergism of adsorption, photocatalysis & photo-ozonation, J. Cleaner Prod., 165 (2017) 431–451.

[7] J. Du, J. Bao, X. Fu, C. Lu, H.K. Sang, Facile preparation of S/Fe composites as an effective peroxydisulfate activator for RhB degradation, Sep. Purif. Technol., 163 (2016) 145–152.

[8] P. Tao, Y. Xu, C. Song, Y. Yin, Z. Yang, S. Wen, S. Wang, H. Liu, S. Li, C. Li, A novel strategy for the removal of rhodamine B (RhB) dye from wastewater by coal-based carbon membranes coupled with the electric field, Sep. Purif. Technol., 179 (2017) 175–183.

[9] A. Kausar, M. Iqbal, A. Javed, K. Aftab, Z.I.H. Nazli, H.N. Bhatti, S. Nouren, Dyes adsorption using clay and modified clay: a review, J. Mol. Liq., 256 (2018) 395–407.

[10] H. Soni, N. Kumar, K. Patel, R.N. Kumar, Photo catalytic efficiency and kinetic studies of ZnO nanoparticles for the removal of basic dye Rhodamine B, Desal. Wat. Treat., 57 (2016) 19857–19864.

[11] S. Venkatesh, A.R. Quaff, N.D. Pandey, K. Venkatesh, Decolorization and mineralization of C.I. direct red 28 azo dye by ozonation, Desal. Wat. Treat., 57 (2016) 4135–4145.

[12] K. Naseem, Z.H. Farooqi, R. Begum, A. Irfan, Removal of Congo red dye from aqueous medium by its catalytic reduction using sodium borohydride in the presence of various inorganic nano-catalysts: a review, J. Cleaner Prod., 187 (2018) 296–307.

[13] G. Sharma, M. Naushad, D. Pathania, A. Kumar, A multifunctional nanocomposite pectin thorium(IV) tungstomolybdate for heavy metal separation and photoremediation of malachite green, Desal. Wat. Treat., 57 (2016) 19443–19455.

[14] G. Sharma, A. Kumar, Mu. Naushad, A. Kumar, A.H. Al-Muhtaseb, P. Dhiman, A.A. Ghfar, F.J. Stadler, M.R. Khan, Photoremediation of toxic dye from aqueous environment using monometallic and bimetallic quantum dots based nanocomposites, J. Cleaner Prod., 172 (2018) 2919–2930.

[15] P. Mazierski, A. Mikolajczyk, B. Bajorowicz, A. Malankowska, A. Zaleska-Medynska, J. Nadolna, The role of lanthanides in TiO_2-based photocatalysis: a review, Appl. Catal., B, 233 (2018) 301–317.

[16] Z.A. Huang, Q. Sun, K. Lv, Z. Zhang, M. Li, B. Li, Effect of contact interface between TiO_2 and g-C_3N_4 on the photoreactivity of g-C_3N_4/TiO_2 photocatalyst: (001) vs (101) facets of TiO_2, Appl. Catal., B, 164 (2015) 420–427.

[17] C. Ottone, A. Lamberti, M. Fontana, V. Cauda, Wetting behavior of hierarchical oxide nanostructures: TiO_2 nanotubes from anodic oxidation decorated with ZnO nanostructures, J. Electrochem. Soc., 161 (2014) 484–488.

[18] A.E. Mragui, I. Daou, O. Zegaoui, Influence of the preparation method and ZnO/(ZnO + TiO_2) weight ratio on the physicochemical and photocatalytic properties of ZnO-TiO_2 nanomaterials, Catal. Today, 321–322 (2019) 41–51.

[19] H. Xu, M. Ding, W. Chen, Y. Li, K. Wang, Nitrogen–doped GO/TiO_2 nanocomposite ultrafiltration membranes for improved photocatalytic performance, Sep. Purif. Technol., 195 (2017) 70–82.

[20] T. Xu, L. Zhang, H. Cheng, Y. Zhu, Significantly enhanced photocatalytic performance of ZnO via graphene hybridization and the mechanism study, Appl. Catal., B, 101 (2011) 382–387.

[21] J. Hu, H. Li, S. Muhammad, Q. Wu, Y. Zhao, Q. Jiao, Surfactant-assisted hydrothermal synthesis of TiO_2/reduced graphene oxide nanocomposites and their photocatalytic performances, J. Solid State Chem., 253 (2017) 113–120.

[22] A. Kumar, A. Kumar, G. Sharma, M. Naushad, R.C. Veses, A.A. Ghfar, F.J. Stadler, M.R. Khan, Solar-driven photodegradation of 17-β-estradiol and ciprofloxacin from waste water and CO_2 conversion using sustainable coal-char/polymeric-g-C_3N_4/RGO metal-free nano-hybrids, New J. Chem., 41 (2017) 10208–10224.

[23] M. Naushad, T. Ahamad, B.M. Al-Maswari, A. Abdullah Alqadami, S.M. Alshehri, Nickel ferrite bearing nitrogen-doped mesoporous carbon as efficient adsorbent for the removal of highly toxic metal ion from aqueous medium, Chem. Eng. J., 330 (2017) 1351–1360.

[24] Inamuddin, S. ul Haque, Mu. Naushad, Electrochemical studies of biocatalytic anode of sulfonated graphene/ferritin/glucose oxidase layer-by-layer biocomposite films for mediated electron transfer, Enzyme Microb. Technol., 87–88 (2016) 29–36.

[25] Inamuddin, K. Ahmad, M. Naushad, Optimization of glassy carbon electrode based graphene/ferritin/glucose oxidase bioanode for biofuel cell applications, Int. J. Hydrogen Energy, 39 (2014) 7417–7421.

[26] R. Begum, Z.H. Farooqi, K. Naseem, F. Ali, M. Batool, J. Xiao, A. Irfan, Applications of UV/Vis spectroscopy in characterization and catalytic activity of noble metal nanoparticles fabricated in responsive polymer microgels: a review, Crit. Rev. Anal. Chem., 48 (2018) 503–516.

[27] C.S. Chou, F.C. Chou, J.Y. Kang, Preparation of ZnO-coated TiO_2 electrodes using dip coating and their applications in dye-sensitized solar cells, Powder Technol., 215–216 (2012) 38–45.

[28] W. Wang, D. Xu, B. Cheng, J. Yu, C. Jiang, Hybrid carbon@TiO_2 hollow spheres with enhanced photocatalytic CO_2 reduction activity, J. Mater. Chem. A, 5 (2017) 5020–5029.

[29] W. Ma, Z. Lu, M. Zhang, Investigation of structural transformations in nanophase titanium dioxide by Raman spectroscopy, Appl. Phys. A, 66 (1998) 621–627.

[30] R. Fagan, D.E. Mccormack, S.J. Hinder, S.C. Pillai, Photocatalytic properties of g-C_3N_4–TiO_2 heterojunctions under UV and visible light conditions, Materials, 9 (2016) 286.

[31] A.G. Ilie, M. Scarisoareanu, I. Morjan, D. Elena, M. Badiceanu, I. Mihailescu, Principal component analysis of raman spectra for TiO_2 nanoparticle characterization, Appl. Surf. Sci., 417 (2017) 93–103.

[32] S. Moradi, P. Aberoomand-Azar, S. Raeis-Farshid, S. Abedini-Khorrami, M.H. Givianrad, The effect of different molar ratios of ZnO on characterization and photocatalytic activity of TiO_2/ZnO nanocomposite, J. Saudi Chem. Soc., 20 (2016) 373–378.

[33] J.J. Zhang, P. Qi, J. Li, X.C. Zheng, P. Liu, X.X. Guan, G.P. Zheng, Three-dimensional Fe_2O_3–TiO_2–graphene aerogel nanocomposites with enhanced adsorption and visible light-driven photocatalytic performance in the removal of RhB dyes, J. Ind. Eng. Chem., 61 (2018) 407–415.

[34] R. Liu, H. Ye, X. Xiong, H. Liu, Fabrication of TiO_2/ZnO composite nanofibers by electrospinning and their photocatalytic property, Mater. Chem. Phys., 121 (2010) 432–439.

[35] C.M. Babu, R. Vinodh, B. Sundaravel, A. Abidov, M.P. Mei, S.C. Wang, H.T. Jang, Characterization of reduced graphene oxide supported mesoporous Fe_2O_3/TiO_2 nanoparticles and adsorption of As(III) and As(V) from potable water, J. Taiwan Inst. Chem. Eng., 62 (2016) 199–208.

[36] X. Cheng, H. Liu, Q. Chen, J. Li, P. Wang, Preparation of graphene film decorated TiO_2 nano-tube array photoelectrode and its enhanced visible light photocatalytic mechanism, Carbon, 66 (2014) 450–458.

[37] M. Sun, Y. Fang, Y. Wang, S. Sun, J. He, Z. Yan, Synthesis of Cu_2O/graphene/rutile TiO_2 nanorod ternary composites with enhanced photocatalytic activity, J. Alloys Compd., 650 (2015) 520–527.

[38] P. Nuengmatcha, S. Chanthai, R. Mahachai, W.C. Oh, Visible light-driven photocatalytic degradation of rhodamine B and industrial dyes (texbrite BAC-L and texbrite NFW-L) by ZnO-graphene-TiO_2 composite, J. Environ. Chem. Eng., 4 (2016) 2170–2177.

[39] G. Sharma, V.K. Gupta, S. Agarwal, S. Bhogal, M. Naushad, A. Kumar, F.J. Stadler, Fabrication and characterization of trimetallic nano-photocatalyst for remediation of ampicillin antibiotic, J. Mol. Liq., 260 (2018) 342–350.

[40] G. Sharma, A. Kumar, S. Sharma, A.H. Al-Muhtaseb, M. Naushad, A.A. Ghfar, T. Ahamad, F.J. Stadler, Fabrication and characterization of novel Fe^0@Guar gum-*crosslinked*-soya lecithin nanocomposite hydrogel for photocatalytic degradation of methyl violet dye, Sep. Purif. Technol., 211 (2019) 895–908.

[41] A. Escobedo-Morales, D. Téllez-Flores, Ma de Lourdes Ruiz Peralta, J. Garcia-Serrano, A.M. Herrera-González, E. Rubio-Rosas, E. Sánchez-Mora, O. Olivares Xometl, Green method for producing hierarchically assembled pristine porous ZnO nanoparticles with narrow particle size distribution, Mater. Chem. Phys., 151 (2015) 282–287.

[42] C. Li, G. Chen, J. Sun, Y. Feng, J. Liu, H. Dong, Ultrathin nanoflakes constructed erythrocyte-like Bi_2WO_6 hierarchical architecture via anionic self-regulation strategy for improving photocatalytic activity and gas-sensing property, Appl. Catal., B, 163 (2015) 415–423.

[43] Y. Hua, C. Wang, J. Liu, B. Wang, X. Liu, C. Wu, X. Liu, Visible photocatalytic degradation of Rhodamine B using Fe(III)-substituted phosphotungstic heteropolyanion, J. Mol. Catal. A: Chem., 365 (2012) 8–14.

[44] C. Yan, K.F. Chen, C.H. Lai, S.W. Lai, Q. Chang, Y.P. Peng, Photocatalytic degradation of Rhodamine B by microwave-assisted hydrothermal synthesized N-doped titanate nanotubes, J. Environ. Sci., 26 (2014) 1505–1512.

[45] B. Dindar, A.C. Güler, Comparison of facile synthesized N doped, B doped and undoped ZnO for the photocatalytic removal of Rhodamine B, Environ. Nanotechnol. Monit. Manage., 10 (2018) 457–466.

[46] X. Ji, C. Bai, Q. Zhao, A. Wang, Facile synthesis of porous SnO_2 quasi-nanospheres for photocatalytic degradation of Rhodamine B, Mater. Lett., 189 (2017) 58–61.

[47] P. Zhang, X. Hua, X. Teng, D. Liu, Z. Qin, S. Ding, CTAB assisted hydrothermal synthesis of lamellar Bi_2WO_6 with superior photocatalytic activity for rhodamine b degradation, Mater. Lett., 185 (2016) 275–277.

[48] H. Liang, Z. Jia, H. Zhang, X. Wang, J. Wang, Photocatalysis oxidation activity regulation of Ag/TiO_2 composites evaluated by the selective oxidation of Rhodamine B, Appl. Surf. Sci., 422 (2017) 1–10.

[49] R. Begum, K. Naseem, E. Ahmed, A. Sharif, Z.H. Farooqi, Simultaneous catalytic reduction of nitroarenes using silver nanoparticles fabricated in poly(*N*-isopropylacrylamide-acrylic acid-acrylamide) microgels, Colloids Surf., A, 511 (2016) 17–26.

[50] F. Bibi, M. Ajmal, F. Naseer, Z.H. Farooqi, M. Siddiq, Preparation of magnetic microgels for catalytic reduction of 4-nitrophenol and removal of methylene blue from aqueous medium, Int. J. Environ. Sci. Technol., 15 (2018) 863–874.

[51] Z. Guo, A. Guo, Q. Guo, M. Rui, Y. Zhao, H. Zhang, S. Zhu, Decomposition of dexamethasone by gamma irradiation: Kinetics, degradation mechanisms and impact on algae growth, Chem. Eng. J., 307 (2017) 722–728.

[52] Z.H. Farooqi, A. Ijaz, R. Begum, K. Naseem, M. Usman, M. Ajmal, U. Saeed, Synthesis and characterization of inorganic–organic polymer microgels for catalytic reduction of 4-nitroaniline in aqueous medium, Polym. Compos., 39 (2018) 645–653.

[53] K. Naseem, Z.H. Farooqi, R. Begum, W. Wu, A. Irfan, A.G. Al-Sehemi, Silver nanoparticles engineered polystyrene-poly(N-isopropylmethacrylamide-acrylic acid) core shell hybrid polymer microgels for catalytic reduction of Congo Red, Macromol. Chem. Phys., 219 (2018) 1800211.

[54] S. Ashraf, R. Begum, R. Rehan, W. Wu, Z.H. Farooqi, Synthesis and characterization of pH-responsive organic–inorganic hybrid material with excellent catalytic activity, J. Inorg. Organomet. Polym., 28 (2018) 1872–1884.

[55] Z. Guo, Z. Zhu, Y. Zhao, H. Cao, F. Liu, Radiolytic decomposition of ciprofloxacin using γ irradiation in aqueous solution, Environ. Sci. Pollut. Res., 22 (2015) 15772–15780.

[56] L. Hu, G. Deng, W. Lu, S. Pang, X. Hu, Deposition of CdS nanoparticles on MIL-53(Fe) metal-organic framework with enhanced photocatalytic degradation of RhB under visible light irradiation, Appl. Surf. Sci., 410 (2017) 401–413.

[57] Z.H. Diao, J.J. Liu, Y.X. Hu, L.J. Kong, D. Jiang, X.R. Xu, Comparative study of Rhodamine B degradation by the systems pyrite/H_2O_2 and pyrite/persulfate: reactivity, stability, products and mechanism, Sep. Purif. Technol., 184 (2017) 374–383.
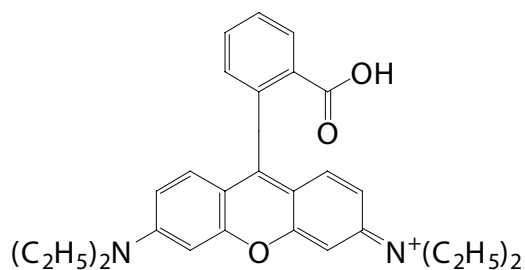
Supplementary Information:
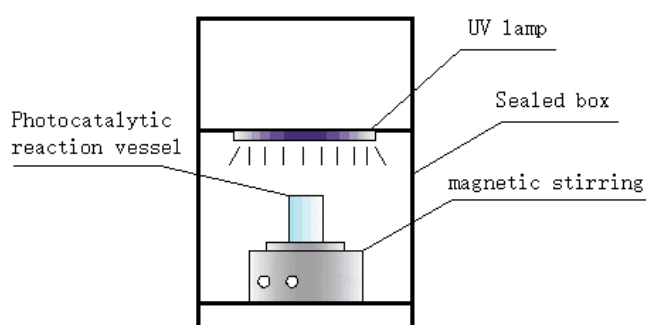

Fig. S1. Structural formula of RhB.

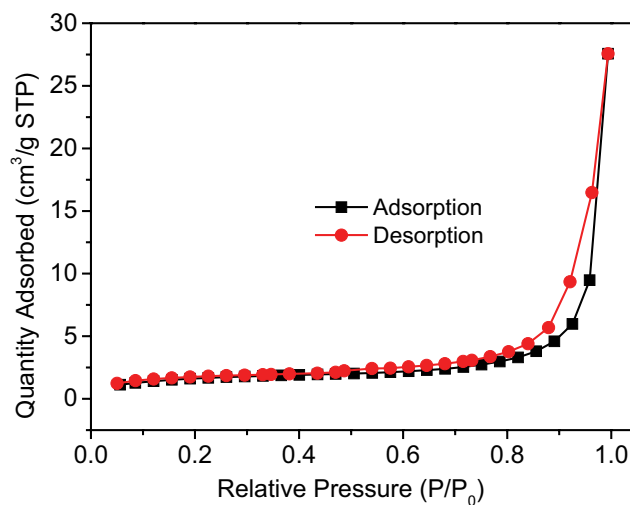Fig. S2. Schematic diagram of the experimental apparatus.

Fig. S3. N_2 adsorption and desorption curve of the TiO_2/ZnO/rGO nanocatalyst.

Table S2
BET surface area, pore volume and pore size of the TiO_2/ZnO/rGO nanocatalyst

BET surface area ($m^2\ g^{-1}$)	Pore volume ($cm^3\ g^{-1}$)	Pore size (nm)
5.72	0.0426	29.78

Table S1
Crystallite dimension of TiO_2 and ZnO in the TiO_2/ZnO/rGO nanocatalyst

Item	2θ	$\cos\theta$	Half-height width B (rad)	Scherrer constant K	X-ray wavelength γ	Average thickness (nm)	Average dimension (nm)
TiO_2	25.3	0.976	0.0033	0.89	0.15418	43	38
	37.8	0.946	0.0030	0.89	0.15418	48	
	48.0	0.914	0.0039	0.89	0.15418	39	
	53.9	0.891	0.0044	0.89	0.15418	35	
	55.1	0.887	0.0045	0.89	0.15418	34	
	62.7	0.854	0.0061	0.89	0.15418	26	
ZnO	31.8	0.962	0.0046	0.89	0.15418	31	31
	34.3	0.956	0.0035	0.89	0.15418	41	
	36.3	0.805	0.0059	0.89	0.15418	25	
	56.6	0.880	0.0063	0.89	0.15418	25	